Particle Acceleration in Relativistic Electron-positron Jets with Helical Magnetic Fields

Meli, Athina; Nishikawa, Kenichi; Dutan, Ioana; Mizuno, Yosuke; Niemiec, Jacek; Gomez, Jose L.; Pohl, Martin; Köhn, Christoph; MacDonald, Nicholas

Published in:
Monthly Notices of the Royal Astronomical Society

Publication date:
2024

Document Version
Early version, also known as pre-print

MNRAS **000**, 1–11 (2020) Preprint 8 September 2020 Compiled using MNRAS LATEX style file v3.0

Particle Acceleration in Relativistic Electron-positron Jets with Helical Magnetic Fields

Athina Meli,[1,2]★ Kenichi Nishikawa,[3] Ioana Duţan,[4] Yosuke Mizuno,[5,6] Jacek Niemiec,[7] Jose L. Gómez,[8] Martin Pohl,[9,10] Christoph Köhn[11] and Nicholas MacDonald[12]

[1]*Space Sciences & Technologies for Astrophysics Research (STAR) Institute Universite de Liege, Sart Tilman, 4000 Liége, Belgium*
[2]*Department of Physics and Astronomy, University of Gent, 9000 Gent, Belgium*
[3]*Department of Physics, Chemistry and Mathematics, Alabama A&M University, Normal, AL 35762, USA*
[4]*Institute of Space Science, Atomiştilor 409, RO-077125 Bucharest-Măgurele, Romania*
[5]*Institute for Theoretical Physics, Goethe University, D-60438 Frankfurt am Main, Germany*
[6]*Tsung-Dao Lee Institute, Shanghai Jiao Tong University, Shanghai, 200240, China*
[7]*Institute of Nuclear Physics Polish Academy of Sciences, PL-31342 Krakow, Poland*
[8]*Instituto de Astrofísica de Andalucía, CSIC, Apartado 3004, 18080 Granada, Spain*
[9]*Institute of Physics and Astronomy, University of Potsdam, 14476 Potsdam-Golm, Germany*
[10]*DESY, Platanenallee 6, 15738 Zeuthen, Germany*
[11]*Technical University of Denmark, National Space Institute (DTU Space), Elektrovej 328, 2800 Kgs Lyngby, Denmark*
[12]*Max-Planck-Institut für Radioastronomie, Auf dem Hügel 69, D-53121 Bonn, Germany*

Accepted Received ; in original form

ABSTRACT

The properties of relativistic jets, their interaction with the ambient environment and particle acceleration due to kinetic instabilities are studied self-consistently with Particle-in-Cell (PIC) simulations. In this work we study how a relativistic $e^{\pm}$ jet containing a helical magnetic field evolves by focusing on its interaction with the external ambient plasma. Particularly, 3D PIC simulations are performed using a longer simulation system than previous studies with an embedded helical magnetic field. An important key issue in this work is how such a magnetic field affects an $e^{\pm}$ jet and how this excites kinetic instabilities such as the Weibel instability (WI), the kinetic Kelvin-Helmholtz instability (kKHI) and others by further focusing on how particles accelerate. We do find that kinetic instabilities along with generated magnetic turbulence are present and consequently accelerate particles. At the linear stage we observe recollimation-like features at the center of the simulated jet and later-on as the $e^{\pm}$ jet evolves, the magnetic fields generated by the instabilities become untangled and reorganized into a new topology near the non-linear phase. We additionally report indications of reconnection near the end of the non-linear stage, before the magnetic-field becomes untangled, as electrons get accelerated by multiple magnetic islands in the jet. In the present study the untangled magnetic field becomes turbulent without any reformation as it happened in our previous study of an $e^{-} - p^{+}$ jet, which we will use to additionally compare the present results, obtaining important insights about the nature of these phenomena applicable to high-energy astrophysical environments such as Active Galactic Nuclei jets and Gamma-ray bursts.

Key words: simulations, acceleration of particles, jets, plasma outflows, relativistic, magnetic reconnection, turbulence

1 INTRODUCTION

Relativistic astrophysical jets are ubiquitous in the Cosmos. Most collimated relativistic jets extend between several thousand up to millions of parsecs (e.g., Blandford et al. 2019) and have been observationally associated with the activity of central black holes in active galactic nuclei (AGN, e.g. EHT Collaboration et al. 2019) and Gamma-ray Bursts (GRBs), as well as with neutron stars or galactic stellar black holes (e.g, Ruiz et al. 2018). The formation and powering of these astrophysical jets is a highly complex phenomenon involving relativistic plasmas and tangled magnetic fields

★ E-mail: ameli@uliege.be

which are organized in such a manner as to ultimately launch an outflow from a central source.

Particle-in-Cell (PIC) and other simulation approaches for studying these jets, and particularly unmagnetized or magnetized relativistic jets which interact with the interstellar medium, have been used for over two decades and have offered tremendous insights into understanding the instabilities, turbulence, and shocks that can develop in the out-flowing plasma leading to particle acceleration and the production of non-thermal radiation (e.g., Giannios et al. 2009; de Gouveia Dal Pino et al. 2010; Uzdensky 2011; Granot 2012; McKinney & Uzdensky 2012; Sironi et al. 2015; Ardaneh et al. 2016; Kadowaki et al. 2018, 2019; Christie et al. 2019; Fowler et al. 2019).

Relativistic jets interact with the plasma environment of an astrophysical source and many instabilities occur, which are responsible for the acceleration of particles. In some cases, e.g., when the jet is unmagnetized, previous computer simulations have shown that the Weibel instability (WI) mediates occasionally relativistic shocks resulting in the acceleration of particles. On the other hand, other instabilities such as the kinetic Kelvin-Helmhotz (kKHI) and mushroom instability (MI) are both created due to the velocity-shear at the boundary between the jet and the ambient medium. Consequently, these instabilities contribute to the generation of magnetic turbulence. PIC simulation studies of the WI, kKHI and MI in slab jet simulations have been investigated and several other studies have been performed concerning the evolution of cylindrical jets with a helical magnetic field topology (e.g., Sironi et al. 2013; Nishikawa et al. 2014; Alves et al. 2015; Nishikawa et al. 2019). The present investigation has been carried out to better understand the nature of particle acceleration in these relativistic plasma flows.

Particles accelerate and radiate within the jet. One possible mechanism of particle acceleration is magnetic reconnection, in which the magnetic topology is rearranged and the magnetic energy is converted into thermal and particle kinetic particle energy. Magnetic reconnection is observed in solar and planetary magnetospheric plasmas and it is often assumed to be an important mechanism of particle acceleration in AGN and GRB jets (e.g, Drenkhahn & Spruit 2002; de Gouveia Dal Pino & Lazarian 2005; Uzdensky 2011; Zhang & Yan 2011; Granot 2012; McKinney & Uzdensky 2012; Giannios 2010, 2011; Komissarov 2012; Sironi et al. 2015; de Gouveia Dal Pino et al. 2018; Kadowaki et al. 2018, 2019; Christie et al. 2019; Fowler et al. 2019).

Magnetic reconnection has been commonly studied with PIC simulations using the Harris model in a slab geometry showing significant particle acceleration (e.g., Zenitani & Hoshino 2005; Oka et al. 2008; Daughton 2011; Kagan et al. 2013; Wendel et al. 2013; Karimabadi et al. 2014; Sironi & Spitkovsky 2014; Guo et al. 2015, 2016a,b). Nevertheless, these studies cannot be directly applied to astrophysical relativistic jets, since the helical magnetic field is believed to be the dominant component of the jet's topology close to the collimation point, as it is shown through observations (Hawley et al. 2015; Gabuzda 2019) as well as MHD modelling Tchekhovskoy (2015).

An overall understanding of the jet physics should emerge from *global* 3D PIC modelling that would allow the investigation of the combined shock/shear processes at the kinetic level. Such studies have first been performed by us for unmagnetized jets (Nishikawa et al. 2016a); in Nishikawa et al. (2016b) we used PIC simulations for the first time to study global magnetized jets with helical magnetic fields. These initial studies analysed jets in both electron-proton and electron-positron pair plasmas, but used limited-size computational boxes. Presently, we extend these studies to larger systems with jets containing a helical magnetic field.

In (Nishikawa et al. 2020) we investigated the evolution of a relativistic electron-proton ($e^- - p^+$) jet containing a helical magnetic field, focusing on the interaction with the ambient plasma, by performing 3D PIC simulations of a jet of relatively large radius in order to examine how the helical magnetic field influences kinetic instabilities (e.g. kKHI, WI and MI) resulting in particle acceleration.

In the present work we extend our study to a relativistic $e^\pm$ jet containing a helical magnetic field. The study involves a larger jet radius and longer simulation times than previous work, allowing for nonlinear evolution and designed to address the following key questions: (i) How does the helical magnetic field affect the growth of kKHI, MI, and WI within the jet, (ii) how do these effects differ in comparison to an $e^- - p^+$ jet, and (iii) how and where are particles accelerated within the jet? Moreover, we will investigate the role of possible magnetic reconnection and will examine the effect of the rapid merging and breaking of the helical magnetic field carried by the jet, as observed in previous studies (e.g., Nishikawa et al. 2016a). We examine the role of potential magnetic reconnection events in a cylindrically injected jet with a helical magnetic field, based on our innovative approach (e.g., Nishikawa et al. 2016b, 2017), with which we previously investigated much smaller systems that exhibited recollimation-like instabilities occurring at an early stage of the simulation. Note that in this previous work, the evolution of $e^\pm$ jets was shaped by a kinetic instability that made the general structure similar to that obtained by our previous work in a simulation study without helical magnetic fields Nishikawa et al. (2016a).

As the magnetic-field structure and particle composition of relativistic jets is still not well understood, this systematic endeavour of simulation studies will provide an advanced and detailed understanding of the magnetic field evolution, possible reconnection events, and particle acceleration applicable to AGN and GRB jets. It is important to note that the differences in the evolved magnetic field structures between jets composed of $e^- - p^+$ and $e^\pm$, could contribute significantly to studies of the polarized emission from AGN jets and GRBs. Particularly, circular polarization (measured as the Stokes parameter V) in the continuum radio emission from AGN jets provides a powerful diagnostic tool of magnetic structures and particle composition because, unlike linear polarization, circular polarization is expected to remain almost completely unmodified by external screens (e.g., O'Sullivan et al. 2013).

It is important to stress out, as discussed in (Nishikawa et al. 2020) for an $e^- - p^+$ jet, that our simulations do not address the large-scale plasma flows of macroscopic parsec-scale jets, but instead they explore relevant kinetic-scale physics within relativistic jet plasmas, which cannot be studied with pure magnetohydrodynamic (MHD) simulations. Therefore, our study is complementary to MHD models and yields important insights into the kinetics at work in relativistic astrophysical jets (see also Nishikawa et al. 2020).

This paper is organized as follows: In Section 2 we describe the details of the set-up of our numerical calculations. In Section 3 we present our results in comparison to the recent work of Nishikawa et al. (2020), and in Section 4 we summarize our conclusions.

2 NUMERICAL APPROACH OF THE SIMULATION SET-UP

We use a 3D PIC code which is a modified version of the relativistic electromagnetic PIC code TRISTAN (Buneman 1993) with MPI-based parallelization (Niemiec et al. 2008; Nishikawa et al. 2009). We apply Cartesian coordinates on a numerical grid of size $(L_x, L_y, L_z) = (1285\Delta, 789\Delta, 789\Delta)$, where $\Delta(= 1)$ is the size of the grid cells. Open boundaries are used on the $x/\Delta = 0$ and $x/\Delta = 1285$ surfaces. Periodic boundary conditions are implemented along the transverse directions y and z. Since the jets are located in the center of simulation box far from the boundaries (see below) and since the simulation is rather short, the effect of periodic boundaries is minimal. Moreover, we have conducted tests which have shown no visible effects of the periodic boundary conditions.

A cylindrical jet containing a helical magnetic field is injected into an ambient plasma and propagates in the x-direction, as shown schematically in Fig. 6a of (Nishikawa et al. 2019). The structure of the helical magnetic field is implemented as in the relativistic MHD (RMHD) simulations of Mizuno et al. (2014). Its components are described in Equations (1) and (2) of Mizuno et al. (2014):

$$B_x = \frac{B_0}{[1 + (r/a)^2]}, \quad B_\phi = \frac{(r/a)B_0}{[1 + (r/a)^2]}, \tag{1}$$

where r is the radial coordinate in cylindrical geometry, B_0 parametrizes the magnetic field strength, and a is the characteristic radius of the magnetic field (Nishikawa et al. 2019) which we assume to be $a = 0.25 \cdot r_{\rm jet}$ ($r_{\rm jet} = 100\Delta$).

As in Mizuno et al. (2014) we choose a constant magnetic pitch and magnetic helicity. The toroidal component of the magnetic field in the jet has a peak value at $r = a$ and is created by an electric current, $+J_x(y, z)$, in the positive x-direction. In Cartesian coordinates the corresponding B_y and B_z field components are defined as:

$$B_y(y, z) = \frac{((z - z_{\rm jc})/a)B_0}{[1 + (r/a)^2]}, \quad B_z(y, z) = -\frac{((y - y_{\rm jc})/a)B_0}{[1 + (r/a)^2]}. \tag{2}$$

The jet Lorentz factor is set to $\gamma_{\rm jt} = 15$, and the jet is initially weakly magnetized while the ambient medium is unmagnetized. The jet's magnetic field amplitude, $B_0 = 0.1c$, corresponds to a plasma magnetization $\sigma = B^2/(n_{\rm e} m_{\rm e} \gamma_{\rm jt} c^2) = 2.8 \times 10^{-3}$, $r_{\rm jet} = 100\Delta$ is the jet radius, and the jet is injected at $x = 100\Delta$ in the center of the $y - z$ plane at $(y_{\rm jc}, z_{\rm jc})$, giving $r = \sqrt{(y - y_{\rm jc})^2 + (z - z_{\rm jc})^2}$, propagating along the x direction.

We follow the jet over a long computational time, $t_{\rm max} = 1000\omega_{\rm pe}^{-1}$, to investigate the nonlinear stage of its evolution. The longitudinal box size, L_x, is twice that in our previous simulation studies (Nishikawa et al. 2016b, 2017, 2019). Equation (2) describes the helicity of the magnetic field to a left-handed polarity for positive B_0. Moreover at the jet opening, the helical magnetic field is computed without a motional electric field. This corresponds to a toroidal magnetic field generated by jet particles moving in $+x$-direction.

For the field external to the jet we use a damping function,

$$\Theta(r - r_{\rm jet}) = \exp\left[-\frac{(r - r_{\rm jet})^2}{b}\right], \text{ where } r > r_{\rm jet} \tag{3}$$

that multiplies the expressions in Equation (2) with tapering parameter $b = 200$. Profiles of the resulting helical magnetic field components are shown in Fig. 6b of Nishikawa et al. (2019) demonstrating that the toroidal magnetic field becomes zero at the center of the jet (red line of Fig. 6b) (see B_ϕ in Eq. (1)).

As in (Nishikawa et al. 2020) the jet head profile in the simulations has a flat-density-top-hat shape. Although the realistic structure of the jet head is far more complex than that, our results are one step in a series of numerical refinements (including the implementation of a Gaussian profile) designed to study PIC jet formations.

In (Nishikawa et al. 2020) we studied an $e^- - p^+$ jet and in this present work we will investigate the same simulation set-up for an $e^\pm$ pair jet. We will show that different plasma compositions exhibit distinct dynamical behavior, which leads to distinct morphologies in the jet evolution as well as in the acceleration and consequent emission of particles.

The initial number densities measured in the simulation frame are $n_{\rm jt} = 8$ and $n_{\rm amb} = 12$, respectively, for pairs in the jet and electrons and positrons in the ambient plasma. Here the electron mass $m_{\rm e}$ is equal to the positron mass $m_{\rm positron}$. For the electron-proton jet, electrons and protons are both in the jet and ambient plasma. The Debye length for ambient electrons is $\lambda_{\rm D} = 0.5\Delta$ and the electron skin depth is $\lambda_{\rm se} = c/\omega_{\rm pe} = 10.0\Delta$ where c is the speed of light and $\omega_{\rm pe} = (e^2 n_{\rm amb}/(\epsilon_0 m_{\rm e}))^{1/2}$ is the electron plasma frequency. The jet-electron thermal velocity is $v_{\rm jt,th,e} = 0.014c$ in the jet reference frame. The electron thermal velocity in the ambient plasma is $v_{\rm am,th,e} = 0.05c$, and the proton thermal velocities are smaller by a factor $(m_{\rm proton}/m_{\rm e})^{1/2} \approx 42$.

3 RESULTS OF SIMULATIONS OF A JET WITH HELICAL MAGNETIC FIELD

In this section we present simulation results for a jet with helical magnetic fields and an $e^\pm$ pair composition and compare them with recent results for a jet composed of $e^- - p^+$ as in Nishikawa et al. (2020). We are particularly interested in the potential differences in the dynamical behavior, and in the way the jet interacts with its surrounding environment.

Let us start with Figure 1, where the jet is injected from left to right in the middle of the graph (at $z/\Delta = 381$) and at $x/\Delta = 100$; through the center of the jet we show cross-sections of the y-component of the magnetic field, $B_{\rm y}$, with the magnetic field in the $x - z$ plane depicted by arrows, at times $t = 600\,\omega_{\rm pe}^{-1}$ and $1000\,\omega_{\rm pe}^{-1}$, for comparison purposes. The $e^\pm$ pair jet is shown in the panels (a, c) and the $e^- - p^+$ jet in panels (b, d).

For the $e^- - p^+$ composition, as it was presented in the work of Nishikawa et al. (2020), we observe a very strong helical magnetic field in the jet at $t = 1000\omega_{pe}^{-1}$ (at around $400 \lesssim x/\Delta \lesssim 830$), where the amplitude was much larger than the initial field, $B/B_0 \approx 40$. This magnetic field amplification was due to the growth of kKHI and MI and it was observed similarly in the un-magnetized case (Nishikawa et al. 2016a). Presently, in Fig. 1d we see that the field structure is strongly modulated which reflects the growth of kKHI along the jet. Nishikawa et al. (2020) demonstrated that this field collimation is caused by the pinching of the jet electrons toward the center of the jet (Fig. 1d is the same as Fig. 1a in Nishikawa et al. (2020)).

The $e^\pm$ pair jet (Figs. 1a and 1c) exhibits a different magnetic field morphology. The WI is generated initially around $x/\Delta = 400$, as shown by the striped magnetic field in Fig. 1a. The growth time is roughly $400\,\omega_{\rm pe}^{-1}$ and the wave length is about $40\,\Delta$. The MI appears near the center of the jet and near the jet boundary, then the longitudinal kKHI wave modes modulate the magnetic field along the jet simultaneously. The growth time of kKHI and MI is roughly $600\omega_{\rm pe}^{-1}$ and the wave length of kKHI is about 60Δ. Beyond $x/\Delta = 750$, a disruption of the magnetic field of the outer mode of

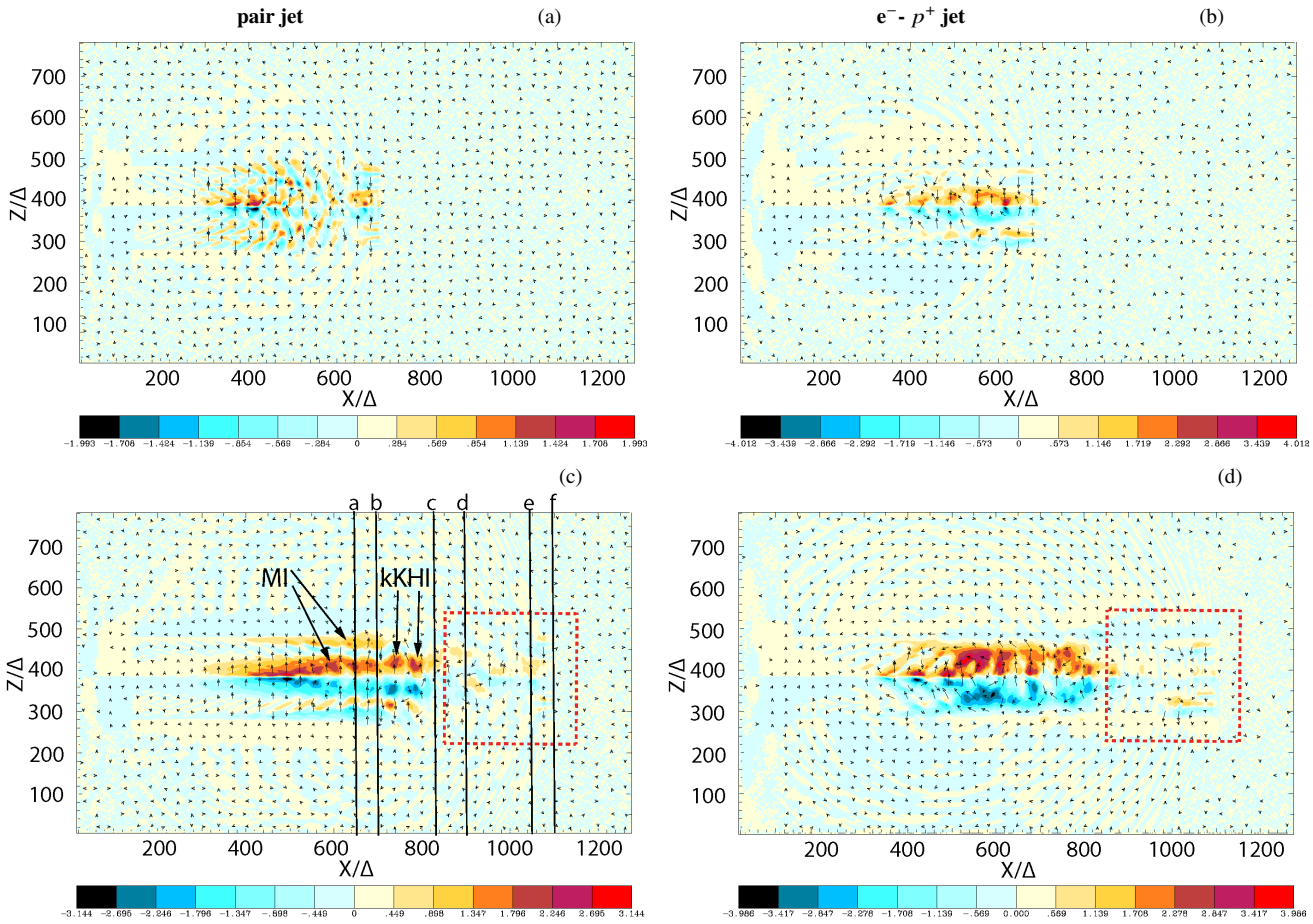

Figure 1. Colormap of the magnetic field amplitude of B_y and the magnetic field components in the $x-z$ plane depicted by arrows, at $t = 600\ \omega_{pe}^{-1}$ (upper panels) and $1000\ \omega_{pe}^{-1}$ (lower panels), respectively. The jet is injected from left in the middle of the $y-z$ plane and at $x = 100\Delta$ and propagates in $+x$-direction. Panels (a, c) are for $e^{\pm}$ plasma while panels (b, d) are for the $e^- - p^+$ case. The dotted squares indicate the volumes plotted in Fig. 4.

MI occurs which results in disordering via a nonlinear saturation of kKHI & MI that is seen, up to $x/\Delta \approx 950$. Firstly, around $x/\Delta = 780$, the magnetic field near the jet boundary disappears; then afterwards the magnetic field gets untangled around $x/\Delta = 820$ (Blandford et al. 2017).

Furthermore, Figure 1c shows the growing kKHI and MI (and WI) generation of two modes of MIs (indicated by two lines), along the jet radius (z). Note here that in the following description (i.e. Figs. 3, 7, 5) we will show nodes of growing MI poloidal to the jet center, following the vertical lines shown in Figure 1c here, and indications of particle acceleration).

Since reconnection in a 3D simulation with a helical magnetic field is complicated, it is not easy to determine its location. The magnetic field structure of a reconnection site in 2D simulations consists of X and O shapes which can be recognized easily. We need to rely on the changes of the magnetic field direction and the null (very weak) magnetic fields in 2D displays in this work. The complex structures of 3D reconnections have been shown in (e.g., Parnell et al. 2010; Lazarian et al. 2020). In order to determine the reconnection locations analytically, we would need to investigate the eigenvalues of Jacobian matrix, which is beyond the scope of this report, for more details, see (Cai et al. 2007).

Just before $x/\Delta = 800$ (Fig. 1 c) one sees a reversal of the magnetic field near the jet with some independent magnetic structures which show a growth of an MI instability. It seems like the magnetic field is maintained longer than in the $e^- - p^+$ plasma (Fig. 1d). Note that the collimation is generated by the strong poloidal (helical) magnetic field, generated by the MI. At around $x/\Delta = 900$ the helical structure of the jet is distorted and weakened, but also reorganized at the center of the jet, which indicates the existence of a non-linear stage of the MI and kKHI. The MI mode near the jet boundary disappears first, but the inner mode (MI and kMHI) stays longer and later disappears as in our previous paper according to the mechanism which is discussed in (Blandford et al. 2017; Nishikawa et al. 2020). At this point things get interesting as the reorganization seen for the magnetic field, means that we have conditions for the occurrence of a magnetic reconnection. We will discuss this point further down in the following figures.

Figure 2 shows the total magnetic-field strength in the $y-z$ plane at $x/\Delta = 830, 900, 1050, 1100$ (panels a, b, c, d) after $t = 1000\omega_{pe}^{-1}$ for the $e^{\pm}$ jet case which allows us to discuss possible reconnection sites corresponding to the same areas of Fig. 1, by showing the magnetic-field structure in the $y-z$ plane as the jet propagates through our simulation box.

The arrows indicate the magnetic field (B_y, B_z). The initial jet radius (slightly expanded) is located in the box which is shown in Fig 2d therefore the jet is expanded outside the jet as shown in Figs. 2a - 2c. The reconnection location should have a minimum total magnetic field strength, which is a necessary condition and which

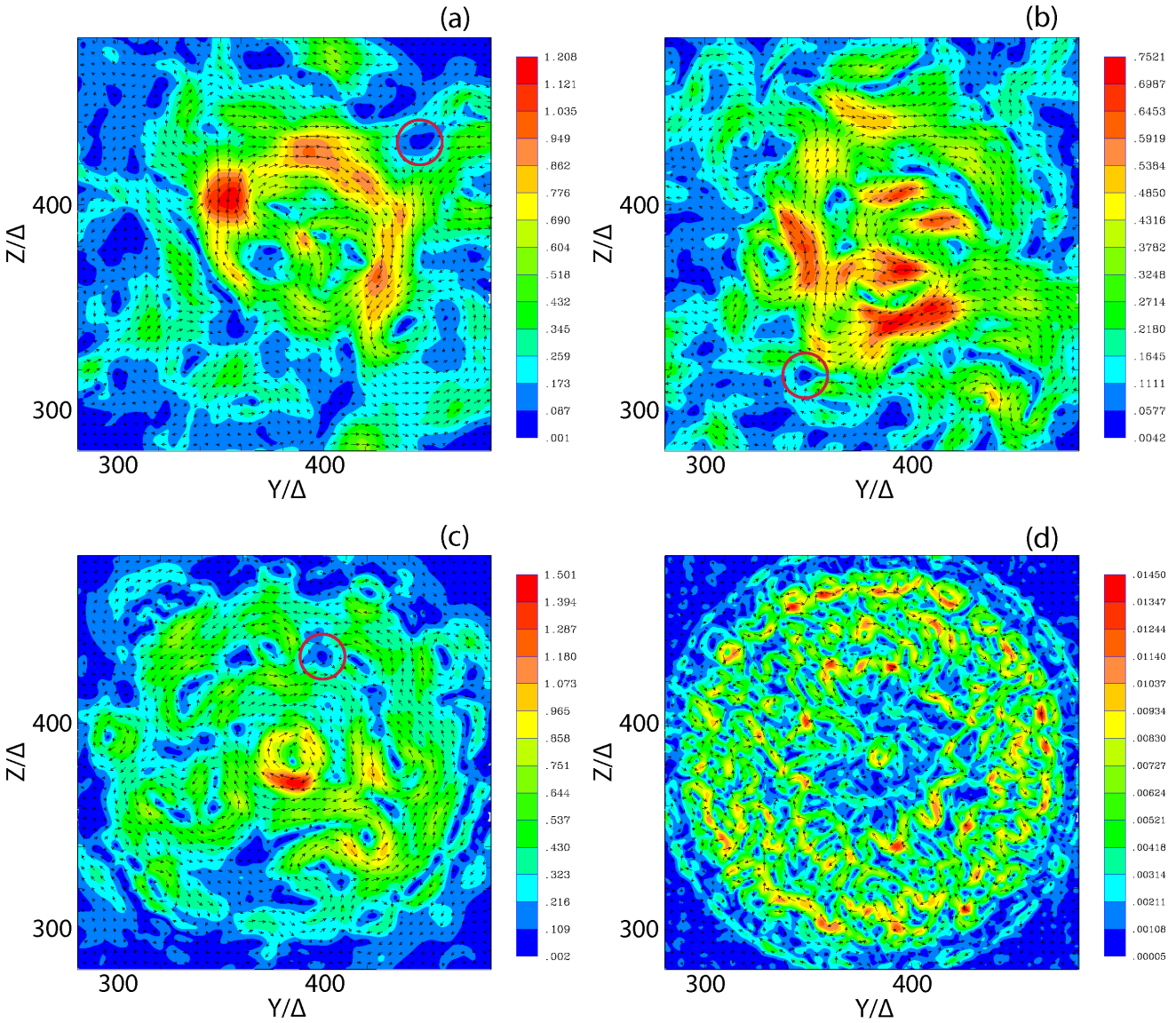

Figure 2. The total magnetic-field strength at time $t = 1000\ \omega_{pe}^{-1}$) is shown for the $e^{\pm}$ pair case in the $y - z$ plane at $x/\Delta = 830, 900, 1050, 1100$ (panels a, b, c, d), respectively, for $281 < y/\Delta, z/\Delta < 481$. The arrows indicate the magnetic field (B_y, B_z).

is indicated by a dark blue colour in the panels. In panels a)-c), we mark examples of possible reconnection sites by red circles.

Fig. 2a shows that at $x/\Delta = 830$ the initially clockwise circular magnetic field starts to split (near the jet) resulting into a number of magnetic structures through the remnants of MIs. These magnetic structures start to get surrounded by opposite polarity fields as we will further show in Fig. 3c below. The magnetic fields are produced by the jet current modified by the excited kKHI and MI. A possible reconnection site is marked by a red circle, where the magnetic fields flux-in from the left and right and flux-out higher and lower. Moving further along the jet to $x/\Delta = 900$ (panel b), one sees a strongly turbulent magnetic field. The helical field structure gets distorted and disperses, as one can also see in the movie provided showing the evolution of the magnetic field at different locations in the jet. The magnetic field is reorganized and forms multiple magnetic islands. The red circle indicates a possible reconnection site where the magnetic fields direct the opposite direction. These processes reflect the non-linear stage of the MI and kKHI. Since the non-linear stage takes over, the instabilities saturate and brake. Note that the evolution in the non-linear stage is different, because the dominantly growing modes are distinct Blandford et al. (2017). The non-linear evolution of the filaments, as one can see in the supplementary video (slideshow), leads to the formation of magnetic field structures which then instigate magnetic reconnection.

We further observe in the panels of Figure 2 and the video (movie3), that the magnetic structures interact with each other and with the surrounding environment generating the right conditions for magnetic reconnection. At $x/\Delta = 1050$ (Fig. 2c) the field starts to get reorganized and examples of possible reconnection sites can be found at $(y/\Delta, z/\Delta) = (400, 435)$ among many other locations where the total magnetic field approaches a null point, with a surrounding magnetic field of the opposite direction.

At the final location $x/\Delta = 1100$ where a full non-linear evolution takes over, we see a complete restoration of the jet boundary

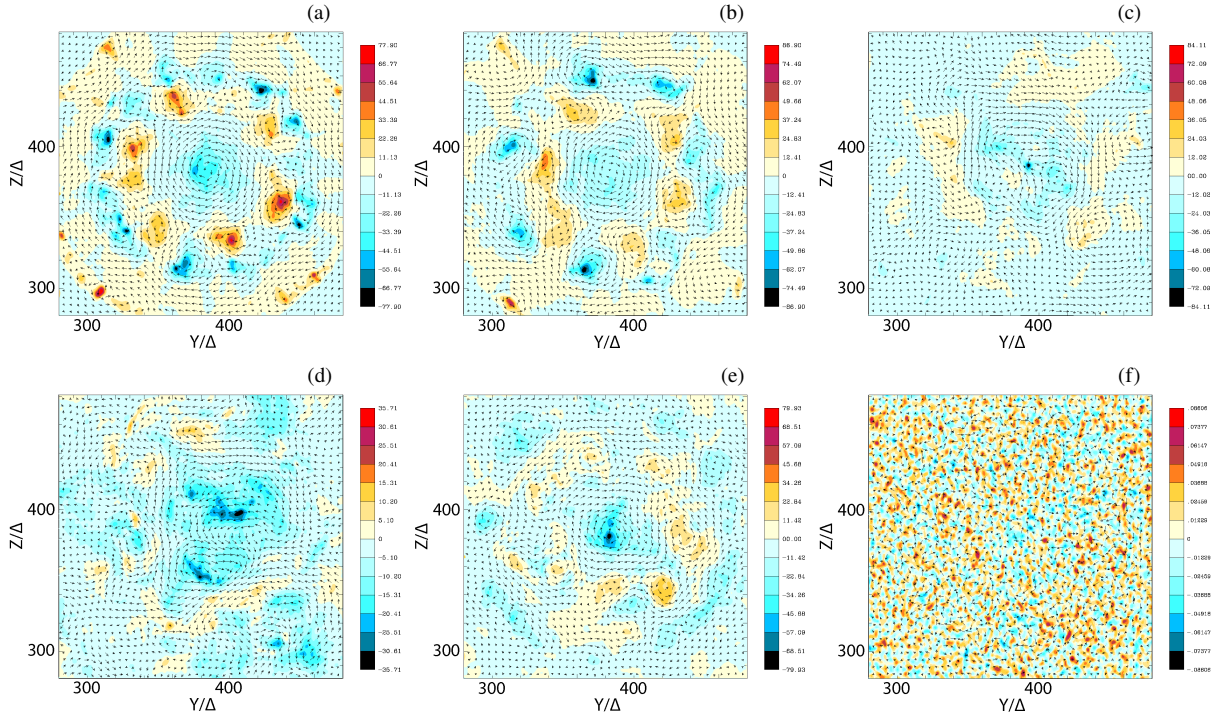

Figure 3. These panels show the x-component $J_{\rm x}$ of the current density with the $B_{\rm y,z}$ (black arrows) for the $e^{\pm}$ case in $x/\Delta = 650, 700, 830, 900, 1050, 1100$ at $t = 1000\,\omega_{\rm pe}^{-1}$.

with a plethora of tiny magnetic islands with almost chaotic orientation of the magnetic field vectors. At the center we observe the reversal of the magnetic field in an anti-clockwise direction with a slight strengthening of the magnetic field. The patterns of the total magnetic fields show the remnants of the growing MI at an earlier stage. Further out there are various small distorted connected islands of a null magnetic field. We note that the filamentary structure at the jet head (Figs. 2d and 1a is formed by the WI (remnants) as it was seen also by Nishikawa et al. (2020). Note that later (in Fig. 4) we will show that in a 3D geometry, a reconnection location can be identified where regions of a weak magnetic field are surrounded by oppositely directed magnetic fields and not by a single x-point, as in a 2D slag geometry here.

Figure 3 shows six 2D isocontour plots at $t = 1000\,\omega_{\rm pe}^{-1}$, for the x-component of the current density, J_x, in the y-z plane with $B_{\rm y,z}$ in black arrows at $x/\Delta = 650, 700, 830, 900, 1050, 1100$ (panels a, b, c, d, e, f) for an $e^{\pm}$ pair jet (corresponding to the vertical black lines of Fig. 1). For an overview of the different properties, we additionally provide two movies for the two different jet compositions ($e^{\pm}$ and $e^{-} - p^{+}$) as supplementary material. It should be noted that in Figs. 3a and 3b two modes of MI, indicated by the two arrows with MI in Fig. 1c along the jet radius (z) in the $x - z$ plane, are recognized through two concentric orange rings with few bunched currents along the poloidal direction (the jet center is located at the middle of panels) in the $y - z$ plane.

Before we move on, we will summarize our understanding about the formation of instabilities in plasma jets. It is known that growing kKHI and MI are observed in jet structures where kKHI have longitudinal modes whilst MI show transverse modes. Thus, one should find the excited modes of kKHI in the $x - z$ plane while the MI modes are found in the $y - z$ plane as shown in Alves et al. (2015); both modes can be seen simultaneously in a 3D graph. Since in our simulations the jet is injected with a sharp edge, this creates by default a discontinuity at the jet boundary which consequently excites kKHI and MI. Inside the jet though, the WI is the instability that is excited due to interaction with the ambient plasma.

In past works it has been found that toroidal magnetic field lines outside of a cylindrical jet, show signatures of kKHI and MI. Specifically, Nishikawa et al. (2014) have shown the development of the MI mode at an earlier linear stage. Then at the non-linear stage as Alves et al. (2012) shown, the MI developed into very large wavelengths with a generation of a DC magnetic field. In Nishikawa et al. (2016a) it was additionally shown that a DC magnetic field becomes more dominant and relates to the collimation of the jet in the $e^{-} - p^{+}$ jet before the non-linear stage. Especially, for relativistic jets with high Lorentz factors the MI is found to be dominant compared to the kKHI. Specifically, for an $e^{\pm}$ pair jet many distinct current filaments are found within the jet due to the small gyroradii of jet electrons and positrons, and are generated near the regions of velocity shear where individual current filaments are wrapped by the magnetic field which indicates the development of MI. This same trend occurs as you have seen previously, in Figs. 1, 2, and 3. Accordingly, the strongly grown MI can be found in Figs. 3a and 3b.

It is known that for an $e^{-} - p^{+}$ jet, waves are generated by the kKHI and the MI. Specifically, layers of concentric rings around the jet seem to be generated by MI. This trend is seen in (Nishikawa et al. 2020) and is used as a comparison with the present study. Specifically, the strongest magnetic fields are generated where the WI develops. One can see clearly the evolution of the currents in the movies, comparing the two cases. The jet protons dominate with strong $+J_x$ currents and concentric rings, maintaining the border of the jet boundaries, contrary to the $e^{\pm}$ pair jet, shown in Fig. 3.

We find that at the first steps along the jet, up to around $x/\Delta = 650$ it seems that a strong helical magnetic field is maintained by a strong J_x by the collimated jet (ambient) electrons, as we have

[h!]

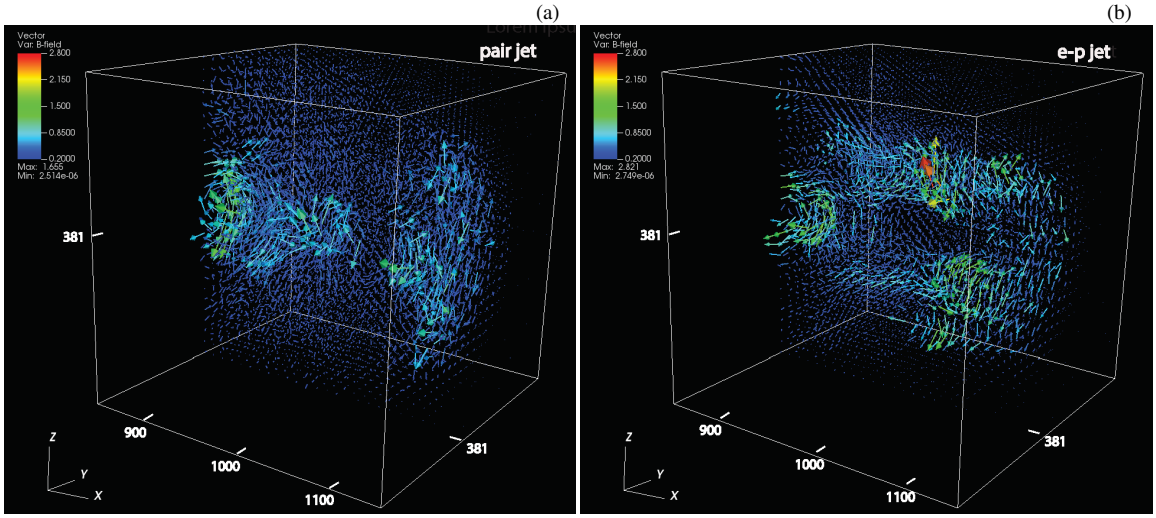

Figure 4. The magnetic field vectors within a cubic section of the simulation grid ($850 < x/\Delta < 1150; 231 < y/\Delta, z/\Delta < 531$) at time $t = 1000\,\omega_{\rm pe}^{-1}$, for $e^{\pm}$ (panel a) and $e^- - p^+$ (panel b). The center of the jet is at $y/\Delta = z/\Delta = 381$. For the magnetic field to be given inside the jet, the plots show half of the regions clipped at the center of jet in the $x - z$ plane ($381 < y/\Delta < 531$).

seen previously in Fig. 1. Once the collimation relaxes, the polarity of the toroidal magnetic fields switches from clockwise to counter-clockwise (Figs. 1c, 1d and Fig. 3d), following the same trend as seen by e.g. Nishikawa et al. (2016a) who have shown that the counter-clockwise magnetic fields were generated by the current layer ($+J_x$) at the jet boundary. Later-on we will show (i.e. Figs. 5) that the due to the perpendicularly accelerated jet electrons in the collimated region, the electrons are expelled from the collimated region and are accelerated-decelerated in a periodic manner due to the growing kKHI. Consequently, the MI is saturated and the strong magnetic field disappears releasing the collimation.

For the $e^{\pm}$ pair jet shown here, Fig. 3 indicates that the small current filaments are generated by the kKHI, MI and the WI as discussed above. Moreover, the slightly stronger current filaments that form and deform periodically and preferentially off the jet-center (seen at the different x snap-shots along the jet and in the movie provided) are most likely generated by the MI. In particular, we can find six modes of MI in Figs. 3a and 3b.

Interestingly, these small current filaments of $-J_x$ eventually merge into the two larger current filaments/magnetic islands, seen more clearly in Fig. 3d. This indicates an occurrence of reconnection in comparison with Fig. 2, where one sees considerable weakening or strengthening of the total magnetic field (B_{tot}) in opposition to the respective J_x almost at around the same areas, which is clearly seen in Fig. 2c, Fig. 3d and Fig. 2d, Fig. 3f.

Fig. 3 also demonstrates that the change of polarity is more prominent at the regime around $x/\Delta = 900$ (see also Fig. 2b), where the distortion and filamentary evolution is more evident, with a followed slight weakening of the magnetic field and a consequent reorganization. The later is evident in Figs. 3b and 3e. One sees smaller islands around the center where anti-clockwise direction of the magnetic field occurs. We observe that the distortion of the magnetic field and the formation of the magnetic structures around the jet center occur earlier than in the $e^- - p^+$ jet (see movie).

Additionally, one finds a wider dispersion of the magnetic fields compared to the $e^- - p^+$ case and the jet border seems to widen more prominently. This happens because of the acceleration of the jet and ambient electrons close to the non-linear stage after the strong collimation effect, as already seen in Fig. 1. It is interesting at this point to note that the current inside the jet starts to weaken towards a null value, therefore the magnetic field is diminishing, evidently in turbulent engulfing magnetic-islands with a counter-clockwise direction, at the later stage (at larger x) more prominently (see Figs. 1 and 2). In addition, one sees that the magnitude of J_x decreases towards a null value in small magnetic structures more prominently in the $e^{\pm}$ jet than what one sees in the $e^- - p^+$ jet case of (Nishikawa et al. 2020). This is what we would expect from a recollimation-like region/shock. Similar behavior can be seen as well in Figs. 1 and 2.

A further comparison of the $e^- - p^+$ and $e^{\pm}$ jet cases shows significant differences in the structure of the jet's current density (J_x), as the reader may clearly see from the movies provided: In an $e^- - p^+$ composition jet, the jet electrons and protons remain closer to the jet border and specifically, currents of protons maintain and frame near the periphery of the jet with occasional concentric rings of $+J_x$. On the other hand, in an $e^{\pm}$ jet the electrons are found outside the jet due to the escape of jet electrons because of the excited instabilities. At the same time the kKHI and MI cause jet and ambient electrons to move away from the jet boundary. This escape of jet electrons occurs because positrons move easily compared to heavier protons. This behavior is consistent with previous simulations (e.g., Nishikawa et al. 2009) of the WI, where current filaments associated with growing instabilities are found in the cross sections of the jet. In particular, for the $e^- - p^+$ case we find that the current filaments lie within the jet, while a negative current is dominant outside the jet. On the other hand, for the $e^{\pm}$ case in Fig. 2, filaments of B_y seem to be found inside and outside the jet. These characteristics are very useful in distinguishing linear or circular polarization signatures in radio maps of AGN jets and other astrophysical relativistic sources.

Figure 4 shows the 3D morphology of the magnetic fields near the jet head. The magnetic-field vectors are shown within a cubic section of the simulation grid at $850 < x/\Delta < 1150$; $231 < y/\Delta, z/\Delta < 531$ at time $t = 1000\,\omega_{\rm pe}^{-1}$, for the $e^{\pm}$ (a) and the $e^- - p^+$ (b) jets. Note that the red-dashed squares in Fig. 1 indicate the same region plotted in these 3D plots. The center of the jet is at

[t!]

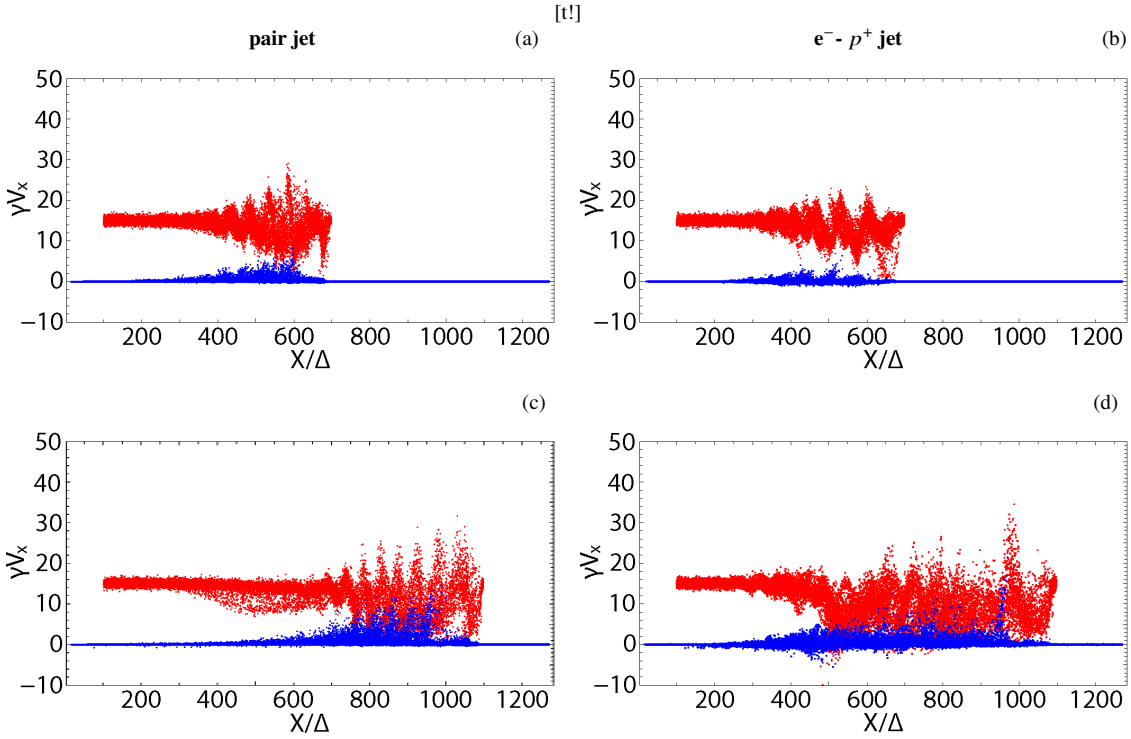

Figure 5. Phase-space $x - \gamma V_x$ distribution of the jet (red) and ambient (blue) electrons, for the $e^{\pm}$ (a, c) jet and $e^- - p^+$ (b, d) jet, respectively, for $t = 600\ \omega_{pe}^{-1}$ (a, b) and $t = 1000\ \omega_{pe}^{-1}$ (c, d). One can easily see that for the $e^{\pm}$ jet the jet electrons are slightly decelerated and that later the kKHI and MI are generated. On the other hand, for the $e^- - p^+$ jet, the MI is excited and jet electrons suddenly decelerate and later, both ambient and jet electrons are accelerated.

$y/\Delta = z/\Delta = 381$. The stronger magnetic fields are generated by the jets, and the plots show half of the regions clipped at the center of jet in the $x - z$ plane with $381 < y/\Delta < 531$.

Before we further discuss Figure 4, let us summarize what was found in the similar simulation study for the $e^- - p^+$ jet case by Nishikawa et al. (2020); hence, we obtain an overall picture of the different physical properties. In Fig. 3 of Nishikawa et al. (2020) it was shown that the edge of the magnetic field of the jet was moving much slower than the jet velocity, which indicates that the front edge of the helical magnetic field is peeled off during the jet propagation. This indicates that the helical magnetic field might have gotten braided by kinetic instabilities and as a consequence it got untangled, as also discussed in Blandford et al. (2017). This condition reveals that the untangling of helical magnetic fields is the result of a magnetic reconnection-like phenomena.

Fig.4b shows that the $e^- - p^+$ jet manifests a tunnel-like feature of a weakened magnetic field at the center of the jet in comparison to the $e^{\pm}$ jet (a). In Fig. 4a, one observes an abrupt weakening of the magnetic field close to a null point, which indicates a reconnection location of the magnetic field at $1000 \leq x/\Delta \leq 1100$ (see also Fig. 2d). For the $e^- - p^+$ case the weakening of the field at the center of the jet is maintained longer, as seen along the $x - y$ plane. For the $e^{\pm}$ jet there is a prominent dispersion (in the $y - z$ plane) of the magnetic field, also at the head of the jet which widens more than what in the $e^- - p^+$ case.

Furthermore, there is a push-out of the helical magnetic fields from the center of the jet at the forward position, where two split smaller magnetic islands are identified. Presently, for the $e^{\pm}$ pair jet one can distinguish smaller magnetic field islands, but close to the jet center in an almost periodic-like pattern. We will see later-on the same trends with the groups of accelerated and decelerated bunches of electrons in the calculated phase-space distributions (i.e. Fig. 5).

It is important to note here that by comparing the previous panels of Fig. 4 with Figs. 1 and 2, the 3D perspectives indicate distinctive differences in the location of the magnetic-islands and vector directions, contrary to the information extracted from the 2D projections of the $y - z$ and $x - z$ planes. The later indicates that one should pay attention to the geometry viewing-angle sensitivity conditions which can be taken under consideration for future studies, combining observational jet polarization maps. In a future work with larger jet systems, we will aim at investigating a comparable case study with astronomical source observables.

Figure 5 shows where electrons are accelerated in the phase space. The phase-space $x - \gamma V_x$ distribution of the jet (red) and ambient (blue) electrons is shown, for the $e^{\pm}$ jet and $e^- - p^+$ jet respectively at $t = 600\,\omega_{pe}^{-1}$ (panels a, b) and $t = 1000\,\omega_{pe}^{-1}$ (panels c, d). One can easily see differences between the time of acceleration of ambient electrons and how both groups of electrons are accelerated at several locations in the $e^{\pm}$ jet. At $t = 1000\ \omega_{pe}^{-1}$ the acceleration location of ambient electrons almost coincides with regions of the jet at $850 < x/\Delta < 1050$ where strong magnetic turbulence is observed, see also Fig. 2, 3 and 4. Note, the maximum acceleration of jet and ambient electrons takes place close to $x/\Delta \sim 1000$, which is more prominent for the $e^{\pm}$ jet rather than for the $e^- - p^+$ jet. Nonetheless, for the $e^- - p^+$ jet there is a slight trend that the maximum electron energy is higher, as we will see later showing the velocity distributions.

We also observe that ambient electrons are strongly accelerated as they are swept up into the relativistic jet plasma. A similar form of electron acceleration occurs during the magnetic-islands

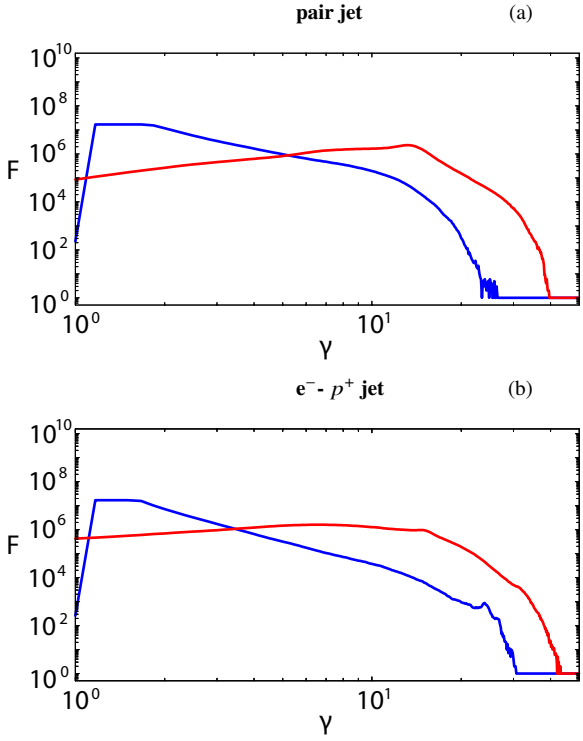

Figure 6. Velocity distributions of the jet (red) electrons and ambient (blue) electrons for the $e^{\pm}$ jet (panel a) and for the $e^{-} - p^{+}$ jet (panel b) for comparison purposes, at $t = 1000\,\omega_{\rm pe}^{-1}$

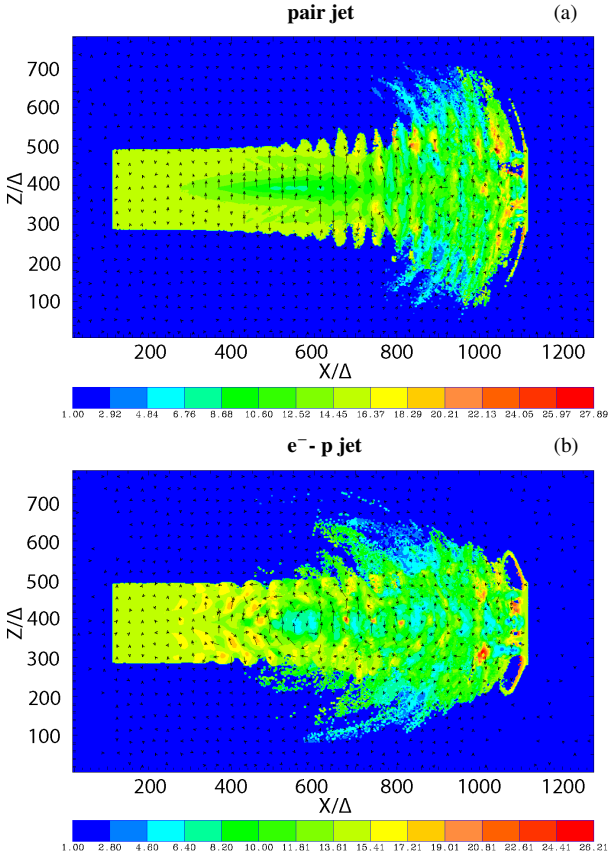

Figure 7. A 2D plot of the Lorentz factor of jet electrons for the $e^{\pm}$ jet (a) and $e^{-} - p^{+}$ (b) jet with $r_{\rm jet} = 100\Delta$ at time $t = 1000\,\omega_{\rm pe}^{-1}$. The arrows show the magnetic fields in the x-z plane.

formation and the weakening/disappearance of the magnetic field, clearly shown in Fig. 2 for the $e^{\pm}$ jet species.

The phase-space distributions at first glance indicate a strong electron acceleration at different locations. Initially the jet electrons have a Lorentz factor of $\gamma \simeq 15$. From Figs. 5a and 5c one observes the following: The distribution of jet electrons (red) in general widens. Specifically, in panel (c) at $t = 1000\,\omega_{\rm pe}^{-1}$, a group of electrons has lower speeds decelerating, but later-on they start an accelerating-decelerating looping in periodical group bunches, eventually reaching maximum energies at $\gamma = 40$, before they start to decelerate again. In comparison with the $e^{-} - p^{+}$ jet case (panel d), the maximum acceleration for the $e^{\pm}$ jet occurs later just after $x/\Delta = 1000$, but at almost the same region of the disappearance of the helical magnetic field. Still the behavior for both cases is slightly different. In terms of the electron acceleration for the $e^{\pm}$ jet (panel c), it is interesting to observe that the ambient electrons are accelerated with the jet electrons after at about $x/\Delta = 800$. A group of electrons accelerates to about $\gamma = 20$ close to $x/\Delta = 1000$, much more prominently than for the $e^{-} - p^{+}$ jet case (panel d). This acceleration coincides almost with the magnetic field weakening seen previously in Fig. 2, where recollimation sites/shocks occur.

Figure 6 shows the velocity distributions of the total jet (red) and ambient (blue) electrons at $t = 1000\,\omega_{\rm pe}^{-1}$ for the $e^{\pm}$ jet (a) and for the $e^{-} - p^{+}$ jet (b). For both jet cases the velocity distribution of the jet electrons shows a flatness peaking close to $\gamma = 15$, which is slightly more prominent for the $e^{\pm}$ jet. Comparing Figs. 6 and 5 indicates that this behavior could be due to the electrons moving swiftly compared to protons which load the jet bulk, giving-off a resulting gradual spectral cut-off, reaching larger energies compared to the ambient electrons.

Additionally, Fig. 6 indicates that the ambient (blue) electrons also show a steeper but clearer power-law distribution, for almost one and a half order of magnitude but with lower cut-offs for $e^{\pm}$ jet: $\gamma = 22$ and $e^{-} - p^{+}$ jet: $\gamma = 30$, which resembles the signature of a stochastic Fermi acceleration mechanism with the power-law shape of cosmic-rays, originated from astrophysical acceleration sites such as jets of AGN and GRBs. Comparing the velocity distributions of panels a and b with the phase-space distributions in Figs. 5c and 5d, we can deduct that the spectral peak of the jet electrons (red) occurs comparably around $x/\Delta = 1000$ which might indicate the further acceleration of jet electrons due to magnetic reconnection. Specifically, at those locations where non-linear phenomena take over, Figure 1c demonstrates that an overall weakening and re-organisation of the magnetic field occurs indicating a reconnection-like event. For the ambient electrons, the same comparison illustrates that the acceleration is more prominent for the $e^{-} - p^{+}$ jet. It will be vital in our next study to run simulations for even larger systems with a larger jet radius such that we are capable of deducting clearer conclusions about these new phenomena.

Upon further inspection of Figs. 5, 6 an interesting property is revealed that might take place with regard to electrons which seem to be able to further accelerate to higher Lorentz factors on account of turbulent acceleration, as in kinetic simulations of driven magnetized turbulence seen in (e.g., Comisso & Sironi 2018; Zhdankin et al. 2018). Note that in these simulations, the turbulent magnetic fluctuations were externally forced in the simulation system, therefore not been self-consistent. In contrast, in our simulations the turbulent magnetic field (where we see multiple magnetic field is-

lands (e.g. in Figs. 1-4) is self-consistently created in the relativistic jets via the simultaneously consistent untangling of the impeded helical magnetic field. Furthermore, the particle acceleration process in turbulent magnetic reconnection has also been examined by, e.g., Kowal et al. (2011, 2012); Lazarian et al. (2016), which supports our argument.

Figure 7 shows the Lorentz factor of the jet electrons for the two jet cases $e^{\pm}$ (a) and $e^{-} - p^{+}$ (b). In both panels the magnetic field's direction is indicated by the black arrows in the $x - z$ plane. The structures seen in both cases at the front-edge of each jet might be generated by the kKHI. Furthermore, it is evident that the kKHI is dominant at $500 < x/\Delta < 880$ in panel (a) while on panel (b) the MI is dominant at around $x/\Delta = 500$. Figure 7a shows that the acceleration of jet electrons occurs along the jet and close to its center due to the stronger collimation around $x/\Delta = 500$. The disruption around the end of the jet is more prominent and expands almost radially as well which creates a Mach cone (bow shock).

Note that in similar simulations, but with smaller systems (Nishikawa et al. 2019), it was found that the Lorentz factor in the $y - z$ plane showed the formation of the MI at the circular edge of the jets.

4 SUMMARY AND DISCUSSION

We have used large-scale 3D PIC simulations to study the properties of relativistic jets, their interaction with the environment, and the behavior of the potential particle acceleration. We examined the potential presence of kinetic instabilities, irregularities and prominent magnetic turbulences, how all these evolve up to the non-linear stage of the simulation and what we can learn from them about the underlying jet kinematics and consequent particle acceleration applicable to a relativistic astrophysical jet environment.

We specifically studied how a relativistic $e^{\pm}$ jet containing a helical magnetic field evolves, focused on how it interacts with the ambient plasma and how particles are accelerated. We found that for a relativistic $e^{\pm}$ jet, kinetic instabilities are indeed present, that the jet boundary is distorted such that the initially embedded helical magnetic field is magnified and untangled when the instabilities are saturated, and that particles are subsequently accelerated by several turbulent magnetic islands/reconnection sites within the jet. Specifically, at the center of the jet at the linear stage, we observed instabilities and later-on as the $e^{\pm}$ jet evolves close to the non-linear stage, the magnetic field becomes extremely turbulent resulting in the formation of magnetic islands of distinctive characteristics. An important point we found is that the untangled magnetic field becomes turbulent without any reformation, as it happened in our previous study of an $e^{-} - p^{+}$ jet. We additionally reported indications of reconnection near the end of the non-linear stage, before the magnetic-field becomes untangled, as electrons get accelerated by multiple magnetic islands in the jet.

Figure 5 shows particle acceleration, however, it is not easy to determine where and how particles are accelerated. The acceleration of particles in turbulent magnetic fields needs further investigation, including the shock drift acceleration (SDA), the shock surfing acceleration (SSA) and the diffusive shock acceleration (DSA), as described in (Matsumoto et al. 2017).

At the non-linear stage it was observed that jet electrons are expanded outside of the jet and the jet boundaries seem to get distorted by the kKHI. Near the jet head of the $e^{\pm}$ jet, as shown in Figs. 3d and 3e, we witnessed a re-arrangement of the magnetic field and a general weakening of the currents with counter-clockwise direction seen from the jet front. We found that at the initial stages along the jet a strong helical magnetic field is maintained by a strong J_x by the collimated jet (ambient) electrons. Then we observed that once the collimation relaxes, the polarity of the toroidal magnetic fields switches from clockwise to counter-clockwise following the same trend as in earlier work of e.g. Nishikawa et al. (2016a), who have calculated that the counter-clockwise magnetic fields are generated by the current layer ($+J_x$) at the jet boundary. We also witnessed the simultaneous acceleration of the jet and ambient electrons (Fig. 5). This kind of behavior is expected when reconnection events occur, which we indeed observed.

Longer simulation runs with larger jet radii will give us even more rigid insights into the new properties of the relativistic jets with embedded helical magnetic fields and their acceleration mechanisms. Although our present work gives important insights already, larger simulations will be needed in order to better understand the evolution of different jet species, the un-tanglement of the helical magnetic field of a relativistic jet, the consequent development of electric and magnetic field irregularities, magnetic islands and reconnection events, which all conclude in assisting the particle acceleration with consequent radiation signatures, which are critical to observational astronomy.

At this point and before closing the conclusions of this study, we will comment on our results in the context of the observational astronomy. It is known that current and magnetic structures are very different for $e^{-} - p^{+}$ and $e^{\pm}$ jet species. The differences arise from the dissimilar mobilities of protons and positrons and these will give different observational signatures in terms of polarity. It has been known by now that the resulting magnetic field structures are different enough to yield distinctive polarizations in VLBI observations of AGN jets at the highest angular resolutions (e.g., Gomez et al. 2016). For example, toroidal magnetic fields (like the helical magnetic field jet in our simulations) inside and outside an $e^{-} - p^{+}$ jet contributes to circular polarization. This will helps us to separate an $e^{-} - p^{+}$ jet clearly from an $e^{\pm}$ jet, at least partially, and also to establish when and if a possible disappearance of the helical magnetic field occurs, in accordance with the present and recent studies (Nishikawa et al. 2020). Moreover, we propose that some of the filaments we report in this work could be observed and verified in the near future with polarimetric VLBI observations at extremely high angular resolutions capable of resolving the transveral structure of the jet, as can be obtained with space VLBI (e.g., Gomez et al. 2016; Giovannini et al. 2018) and millimeter ground-based observations with the Event Horizon Telescope (e.g., EHT Collaboration et al. 2019; Kim et al. 2020). In addition, it will be important to investigate observationally and in-tandem with simulations, the signatures of reconnection phenomena since the dissipation of a significant fraction of the magnetic energy (i.e. reconnection) will naturally result in the appearance of flares from astrophysical source candidates. Particularly, this will happen when an accelerated particle beam is directed along the line of sight, see (Komissarov 2012; McKinney & Uzdensky 2012; Sironi et al. 2015). Our study might have very important implications in this context as, for example, the expected prompt GRB emissions, could be due to reconnection events which can be investigated via the temporal and spectral properties of simulation studies, together with observations. This will be one of our next aims in a follow-up work.

DATA AVAILABILITY

The data underlying this article will be shared on reasonable request to the corresponding author.
The supplementary videos for this publication can be obtained from http://doi.org/10.5281/zenodo.4018699

ACKNOWLEDGMENTS

This work was supported by the NASA-NNX12AH06G, NNX13AP-21G, and NNX13AP14G grants. Recent work was also provided by the NASA through Chandra Award Number GO7-18118X (PI: Ming Sun at UAH) issued by the Chandra X-ray Center, which is operated by the SAO for and on behalf of the NASA under contract NAS8-03060. The work of J.N. has been supported by Narodowe Centrum Nauki through research project 2019/33/B/ST9/02569. Y.M. is supported by the ERC Synergy Grant "BlackHoleCam: Imaging the Event Horizon of Black Holes" (Grant No. 610058). The work of I.D. has been supported by the NUCLEU project. Simulations were performed using Pleiades and Endeavor facilities at NASA Advanced Supercomputing (NAS: s2004), using Comet at The San Diego Supercomputer Center (SDSC), and Bridges at the Pittsburgh Supercomputing Center, which are supported by the NSF. JLG acknowledges the support of the Spanish Ministerio de Economía y Competitividad (grants AYA2016-80889-P, PID2019-108995GB-C21), the Consejería de Economía, Conocimiento, Empresas y Universidad of the Junta de Andalucía (grant P18-FR-1769), the Consejo Superior de Investigaciones Científicas (grant 2019AEP112), and the State Agency for Research of the Spanish MCIU through the "Center of Excellence Severo Ochoa" award for the Instituto de Astrofísica de Andalucía (SEV-2017-0709).

REFERENCES

Alves, E.P., Grismayer, T., Martins, S.F., Fiuza, F., Fonseca, R.A., & Silva, L.O., 2012, ApJ, 746, L14
Alves, E.P., Grismayer, T., Fonseca, R.A., Silva, L.O., 2015, Phys. Rev. E, 92, 021101
Ardaneh, K., Cai, D., Nishikawa, K.I., 2016, ApJ, 827, 124
Blandford, R., Meier, D., Readhead, A., 2019, ARA & A, 57, 467
Blandford, R., Yuan, Y, Hoshino, M., Sironi, L., 2017, Space Sci Rev, 207, 291
Buneman, O. 1993, in *Computer Space Plasma Physics: Simulation Techniques and Software*, Eds.: Matsumoto & Omura, Tokyo: Terra, p.67
Cai, D.S., Nishikawa, K.-I., Lembege, B., 2007, in *Advanced Methods for Space Simulations*, edited by H. Usui and Y. Omura, TERRAPUB, Tokyo, pp. 145â€"166
Christie, I. M., Lalakos, A., Tchekhovskoy, A., Fernandez, R., Foucart, F., Quataert, E., Kasen, D., 2019, MNRAS, 490, 4811
Comisso, L., Sironi, L., 2018, prl, 121, 255101
Daughton, W., Roytershteyn, V., Karimabadi, H., et al. 2011, Physics Nature, 7, 539
de Gouveia Dal Pino, E. M., & Lazarian, A. 2005, A&A 441, 845
de Gouveia Dal Pino, E. M., Piovezan, P. P., Kadowaki, L. H. S. 2010, A&A, 518, 5
de Gouveia Dal Pino, E. M., Alves Batista, R., Kowal, G., Medina-Torrejn, T., Ramirez-Rodriguez, J. C. 2018, https://pos.sissa.it/cgi-bin/reader/conf.cgi?confid=329
Drenkhahn, G., & Spruit, H. C., 2002, A&A 391, 1141
EHT Collaboration, 2019, ApJ, 871, L1
Fowler, T. K., Li, H., Anantua, R., 2019, ApJ, 885, 4
Gabuzda, D., 2019, Galaxies, 7, 5
Giannios, D., Uzdensky, D. A., & Begelman, M. C., MNRAS, 395, L29
Giannios, D., 2010, MNRAS, 408, L46
Giannios, D., 2011, J. Phys: Conf. Ser. 283, 012015
Giovannini, G., et al. 2018, Nature Astronomy, 2, 472
Granot, J., 2012, MNRAS, 421, 2442
Gómez, José L., Lobanov, Andrei P., Bruni, Gabriele, Kovalev, Yuri Y., Marscher, Alan P., Jorstad, Svetlana G., Mizuno, Yosuke, Bach, Uwe, Sokolovsky, Kirill V., Anderson, James M., Galindo, Pablo, Kardashev, Nikolay S., Lisakov, Mikhail M., 2016, ApJ, 817, 96
Guo, F., Liu, Y.-H., Daughton, W., & Li, H., 2015, ApJ, 806, 167
Guo, F., Li, H., Daughton, W., et al., 2016a, ApJL, 818, L9
Guo, F., Li, H., Daughton, W., Li, X., & Liu, Y.-H., 2016b, PhPl, 23, 5708
Hawley, J. F., Fendt, C., Hardcastle, M., et al. 2015, Space Sci. Rev., 191, 441
Kim, J-Y, et al. 2020, A&A, 640, A69
Kadowaki, L. H. S., De Gouveia Dal Pino, E. M., Stone, J. M., 2018, ApJ, 864, 52
Kadowaki, L. H. S., de Gouveia Dal Pino, E. M., Medina-Torrejn, T. E. https://pos.sissa.it/cgi-bin/reader/conf.cgi?confid=329
Kagan, D., Milosavljevic, M., & Spitkovsky, A. 2013, ApJ, 774, 41
Karimabadi, H., Roytershteyn, V., Vu, H. X., et al., 2014, PhPl, 21, 2308
Komissarov, S. S. 2012, MNRAS, 422, 326
Kowal, G., de Gouveia Dal Pino, E.M., Lazarian, A., 2011, ApJ. 735, 102
Kowal, G., de Gouveia Dal Pino, E. M., Lazarian, A., 2012, Phys. Rev. Lett., 108, 241102
Lazarian A., Kowal G., Takamoto M., de Gouveia Dal Pino E.M., Cho J. 2016, Theory and Applications of Non-relativistic and Relativistic Turbulent Reconnection. In: Gonzalez W., Parker E. (eds) Magnetic Reconnection. Astrophysics and Space Science Library, vol 427. Springer, Cham
Lazarian, A., Eyink, G. L., Jafari, A., Kowal, G., Li, H., Siyao Xu, S., and Vishniac, E. T., Phys. Plasmas, 27, 012305, 2020
Matsumoto, Y., Amano, T., Kato, T. N., Hoshino, M., 2017, Phys. Rev. Lett., 119, 105101
McKinney, J. C., & Uzdensky, D. A., 2012, MNRAS, 419, 573
Mizuno, Y., Hardee, P. E., & Nishikawa, K.-I., 2014, ApJ, 784, 167
Niemiec, J., Pohl, M., Stroman, T., & Nishikawa, K.-I., 2008, ApJ, 684, 1174-1189
Nishikawa, K.I.., Hardee, P.E., Du?an, I., Niemiec, J., Medvedev, M., Mizuno, Y., Meli, A., Sol, H., Zhang, B., Pohl, M., et al., 2014, ApJ, 793, 60
Nishikawa, K.-I., Mizuno, Y., Gómez, J. L., et al., 2020, MNRAS, 493, 2652
Nishikawa, K.-I., Frederiksen, J. T., Nordlund, Å., et al., 2016a, ApJ, 820, 94
Nishikawa, K.-I., Mizuno, Y., Niemiec, J., et al., 2016b, Galaxies, 4, 38
Nishikawa, K.-I., Mizuno, Y., Gómez, J. L., et al., 2017, Galaxies, 5, 58
Nishikawa, K.-I., Mizuno, Y., Gómez, J. L., et al., 2019, Galaxies, 7, 29
Nishikawa, K. -I., J. Niemiec, M. Medvedev, H. Sol, P. Hardee,Y. Mizuno, B. Zhang, M. Pohl, M. Oka, D. H. Hartmann, ApJ, 698, L10, 2009
Oka, M., Fujimoto, T. K., Nakamura, M., et al. 2008, PRL, 101, 205004
Ruiz, M.; Shapiro, S. L.; Tsokaros, A., 2018, Physical Review D. 97 (2): 021501.
O'Sullivan, S.P., McClure-Griffiths, N.M., Feain, I.J., Gaensler, B.M., Saul, R.J. Mon. Not. R. Astron. Soc. 2013, 435, 311â€"319.
Parnell, C. E., Rhona C. Maclean, R. C., Haynes, A. L. and Galsgaard, K., Astrophysical Dynamics: From Galaxies to Stars Proceedings IAU Symposium No. 271, 227, 2010
Sironi, L., Spitkovsky, A., Arons, J., 2013, ApJ, 771, 54.
Sironi, L. & Spitkovsky, A., 2014, ApJ, 783, L21
Sironi, L., Petropoulou, M., & Giannios, D., 2015, MNRAS, 450, 183
Tchekhovskoy, A., 2015, ASSL, 414, 45
Uzdensky, D. A., 2011, Space Sci. Rev., 160, 45
Wendel, D. E., Olson, D. K., Hesse, M., et al., 2013, PhPl, 20, 2105
Zenitani, S. & Hoshino, M., 2005, ApJ, 618, L111
Zhang, B. & Yan, H., 2011, ApJ, 726, 90
Zhdankin, V., Uzdensky, D. A., Werner, G. R., Begelman, M. C., 2018, ApJL, 867, L18

This paper has been typeset from a TEX/LATEX file prepared by the author.